Research Square

Preprints are preliminary reports that have not undergone peer review.
They should not be considered conclusive, used to inform clinical practice,
or referenced by the media as validated information.

SGL-CNN: A Dual-Domain Convolutional Neural Network harnessing Spatial and Frequency Features for Bathymetry Estimation

Luting Hua
Jiangxi University of Finance and Economics
Chao Wang
Jiangxi University of Finance and Economics
Jieru Zhan
Jiangxi University of Finance and Economics
Xiaohui Liu
liuxiaohui@jxufe.edu.cn
Jiangxi University of Finance and Economics

Research Article

Keywords: Bathymetry prediction, Gravity anomalies, Convolutional Neural Network, Spatial domain, Frequency domain

Posted Date: April 6th, 2026

DOI: https://doi.org/10.21203/rs.3.rs-9263717/v1

License: This work is licensed under a Creative Commons Attribution 4.0 International License.
Read Full License

Additional Declarations: No competing interests reported.

Version of Record: A version of this preprint was published at Marine Geophysical Research on July 1st, 2026. See the published version at https://doi.org/10.1007/s11001-026-09620-y.

SGL-CNN: A Dual-Domain Convolutional Neural Network harnessing Spatial and Frequency Features for Bathymetry Estimation

Luting Hua[1], Chao Wang[2], Jieru Zhan[1], Xiaohui Liu[2*]

[1]School of Statistics and Data Science, Jiangxi University of Finance and Economics, Shuanggang, Nanchang, 330013, Jiangxi, China.
[2*]Key Laboratory of Data Science in Finance and Economics, Jiangxi University of Finance and Economics, Shuanggang, Nanchang, 330013, Jiangxi, China.

*Corresponding author(s). E-mail(s): liuxiaohui@jxufe.edu.cn;
Contributing authors: HUAluting1780172@outlook.com;
wangchaoanhui@126.com; 2875379662@qq.com;

Abstract

Bathymetric prediction using Convolutional Neural Networks (CNNs) to model the nonlinear relationship between gravity anomalies and seafloor topography has gained significant attention. However, most CNN-based methods operate primarily in the spatial domain, which often results in limited resolution and an inability to recover fine-grained topographic features. To address this, we propose a novel feature engineering framework, spatial global- and local-convolutional neural networks (SGL-CNN), that extracts multi-source input features from both spatial and frequency domains. This architecture enables the integrated "multi-source gravity + long-wavelength" data to simultaneously represent both low- and high-frequency components of the seafloor, facilitating the reconstruction of more detailed topography. The effectiveness of our SGL-CNN model is validated in representative regions of the Western Pacific, including a slope, a seamount, and a trench, against established baseline methods (ParkerO, SAS, GGM, CNN). Results demonstrate that SGL-CNN outperforms the baseline methods in predicting bathymetry over seamounts and trenches. By presenting results across diverse terrains and depth ranges, we show that SGL-CNN's dual-domain architecture effectively handles the multi-scale wavelength distribution of complex seafloor landscapes—recovering low-frequency (slope trends), medium-frequency (seamount bodies), and high-frequency (trench fracture zones) components. This

capability overcomes the spectral truncation issue common in single-domain methods, enabling high-resolution bathymetric inversion.

Keywords: Bathymetry prediction; Gravity anomalies; Convolutional Neural Network; Spatial domain; Frequency domain

1 Introduction

High-resolution seafloor topography is crucial for marine science, resource exploration, economic development, and defense. Shipborne sonar is the main method for obtaining bathymetric data, having advanced from single-beam to multi-beam systems that measure depth in swaths rather than points, significantly enhancing survey accuracy and resolution [1–3] . So far, the Seabed 2030 project has mapped over 20% of the global seafloor at 400-meter resolution [4–6]. Yet, shipborne sonar surveys are time-consuming, limited in coverage, and resource-intensive. Completing global mapping with sounding only would take roughly 900 ship-years of continuous effort [7].

The advancements of satellite altimetry has facilitated the generation of global, uniformly resolved gravity anomaly maps, offering an alternative to shipboard echo sounding for constructing seamless seafloor maps [8, 9]. Bathymetric prediction methods from gravity anomalies broadly fall into two categories. Frequency-domain techniques [1, 10–12], pioneered by [10] and [11], utilize the iterative principles of potential fields to relate gravity anomalies to seafloor undulations. Building on this, the SAS method [1] decomposes bathymetry into spectral components, deriving medium- and short-wavelength topography from filtered gravity anomalies and integrating it with a long-wavelength model from sparse ship measurements, and have consequently generated a series of topographic products, such as SRTM15+ [13, 14]. Spatial-domain techniques, meanwhile, include the classical gravity-geologic method [15, 16] and a growing number of artificial intelligence methods that are attracting increasing research interest [6, 17, 18], which can effectively capture the nonlinear relationship between gravity anomalies and seafloor topography.

Additionally, an increasing number of studies are combining spatial domain GGM with neural network approaches, using GGM to decompose gravity anomalies into wavebands as more precise input features [19–21], where gravity anomalies are decomposed into long-wavelength and short-wavelength components. The long-wavelength components reflect low-frequency information of the topography, and the short-wavelength components reflect high-frequency information of the topography [22]. The "GGM + Neural Network" series of methods not only consider the nonlinear relationship between seafloor topography and gravity information but also utilize multi-source long-wavelength and short-wavelength gravity information to more comprehensively reflect variations in seafloor topography, thereby aiding in the construction of high-resolution seafloor maps.

Existing methods, which operate predominantly in either the spatial or frequency domain, fail to integrate global and local features simultaneously. Spatial-domain

approaches, such as GGM and direct CNNs, are computationally intensive and rely primarily on local features, lacking a global perspective—limiting the resolution and generalizability of the predicted bathymetry [3, 23]. Frequency-domain methods, by contrast, are computationally efficient and leverage global features from gravity anomalies, but they overlook local features due to spectral truncation and heavy reliance on manual filter selection [1, 10]. Integrating the strengths of both domains to achieve high-resolution bathymetric inversion thus remains a critical and unresolved challenge.

To extract both global and local features from the input gravity anomalies, we propose a novel feature engineering framework, SGL-CNN, which integrates multi-scale information from the spatial and frequency domains adaptively. Building upon multi-source gravity data and inspired by the SAS methodology [1], we incorporate long-wavelength bathymetry as an additional input feature, introducing another key novelty. The SGL-CNN architecture effectively models nonlinear relationships within 2D gridded data by: (1) extracting spatial features directly from raw gravity signals and long-wavelength topography; (2) decomposing all input grids into frequency bands via Fourier transform to capture global spectral information; and (3) extracting local frequency-domain features through sliding window analysis.

The remainder of this paper is structured as follows. Section 2 introduces the architecture of the proposed spatial global- and local-CNN (SGL-CNN), detailing its three specialized branches for spatial feature extraction, global frequency analysis, and local frequency analysis. The experimental design is outlined in Section 3, where three representative regions — slope, seamount, and trench — are selected to test SGL-CNN, alongside several baseline methods (Parker-O, SAS, GGM, CNN) for a comprehensive comparison. Section 4 provides a thorough validation, demonstrating SGL-CNN's effectiveness in seafloor recovery through a comparative analysis of prediction deviations across depth ranges and an evaluation of restored frequency components via power spectral density (PSD).

2 Methodology and Techniques

2.1 The Proposal of Multiple Scales

Gravity anomalies at the sea surface arise from seafloor topographic undulations, which perturb the sea surface height and thus the gravitational field. As illustrated in Fig. 1, the spatial scale of the resulting gravity anomaly depends on the depth of the topographic feature. The main aspects of this relationship can be summarized as follows:

- **From sea surface height to gravity anomalies: the role of scale.** In deeper waters, topographic undulations produce sea surface height variations over larger spatial scales, while in shallower waters they generate variations over smaller scales [24]. Different scales of sea surface height correspond to different integration ranges in the gravity anomaly calculation, thus contributing to gravity anomalies of distinct wavelengths. As shown in Fig. 1, the similar topographic undulations located at

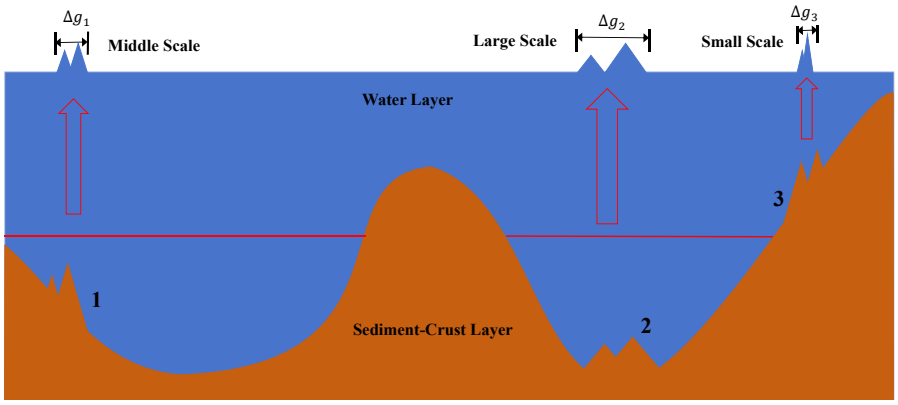


Fig. 1: Spatial scale characteristics of gravity anomalies arising from topographic features at different elevations. The wavelength of the induced gravity signal decreases with increasing source depth, illustrating the multiscale nature of bathymetric gravity signals.

different elevations result in sea surface height ranges of different spatial scales, which in turn induce gravity anomalies of different magnitudes.

- **Multi-scale gravity anomalies in the spatial domain.** Gravity anomalies are fundamentally generated by the undulations of seafloor topography. The nonlinear relationship between sea-surface gravity anomalies and seafloor topography affects gravity observations within a given spatial range. For each grid point on the sea surface, one should not consider only the gravity anomaly derived from a single scale of bathymetric variation. Instead, contributions from multiple scales must be taken into account, giving rise to multi-scale gravity anomalies in the spatial domain.
- **Frequency domain representation for global features.** In the frequency domain, gravity anomalies are decomposed into different wavelength bands, where low-frequency (long-wavelength) components capture the large-scale, global topographic trends, while high-frequency (short-wavelength) components reflect local bathymetric details. This decomposition provides a natural way to extract global features efficiently, a key advantage of frequency-domain methods. By jointly considering the full spectral content, the frequency domain offers a comprehensive characterization of the gravity field that complements spatial-domain analysis.
- **Long-wavelength topography from ship soundings.** Short-wavelength seafloor features can be inverted directly from gravity anomalies, whereas the long-wavelength (background) topography is typically derived by low-pass filtering sparse shipborne bathymetry. Because this long-wavelength component is inherently coarse and limited by the coverage of ship surveys, it requires multiscale trend extraction in both the spatial and frequency domains when used as input—analogous to the processing of gravity anomalies.

In summary, leveraging multi-source [1] gravity anomalies and long-wavelength bathymetry across both the spatial and frequency domains is essential for accurately mapping seafloor topography.

2.2 Methodology Framework

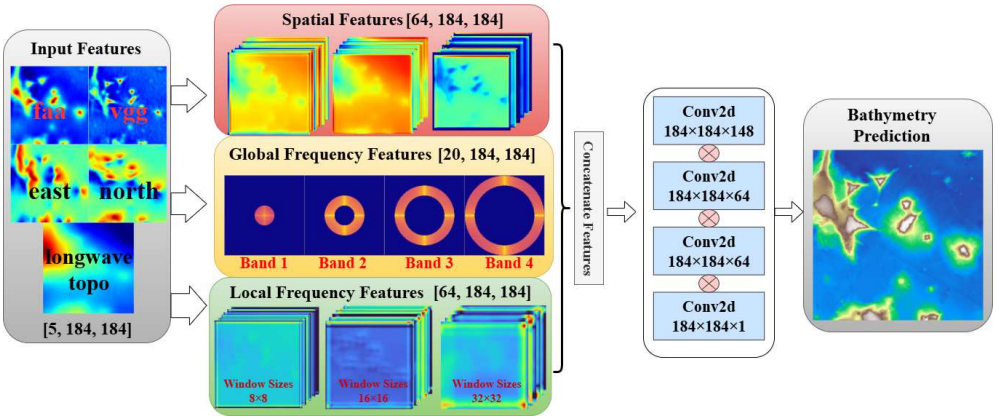


Fig. 2: The architecture of SGL-CNN

As illustrated in Fig. 2, the method accepts five input gridded features at 1-arc-minute resolution:

(i) Free-Air Gravity Anomaly (*faa*),
(ii) Vertical Gravity Gradient (*vgg*),
(iii) East-West components of deflection of the vertical (*east*),
(iv) North-South components of deflection of the vertical (*north*),
(v) Long-wavelength bathymetry (*long-topo*).

For each $3° \times 3°$ study region, we perform a perimeter expansion by extending the input features by one grid cell outward in all four directions. At 1-arc-minute resolution, a $3° \times 3°$ region originally contains 180×180 grid cells; the expansion adds two cells on each side, resulting in a final grid size of 184×184 cells. This operation helps mitigate edge effects when extracting local frequency-domain features via sliding windows. The five expanded feature maps are stacked to form an input tensor $\mathbf{X} \in \mathbb{R}^{5\times184\times184}$, where the dimensions correspond to (channels, height, width).

The input tensor is simultaneously processed by three parallel feature extraction branches, each designed to capture multiscale information from a distinct perspective:

[1] Here, "multi-scale" refers to the decomposition of signals into contributions from different spatial or spectral bands—a fundamental step for separating the effects of the gravity field and long-wavelength topography on bathymetric predictions.

(a) Spatial feature branch – employs convolutional kernels to extract local spatial patterns at multiple scales directly from the input grids.
(b) Global frequency feature branch - applies the Fourier transform to the full spatial extent of each input, decomposing it into spectral bands to capture long-wavelength (global) information.
(c) Local frequency feature branch – performs Fourier transforms on sliding local windows, extracting short-wavelength (local) information from spectral features across the domain of each input.

Together, these branches extract complementary multiscale features—spatial, global frequency, and local frequency. By synergistically integrating these three complementary representations—spatial features preserving topographic continuity, global frequency features capturing periodic geological patterns, and local frequency features enhancing fine-scale details—the fused multi-branch architecture achieves comprehensive bathymetry prediction. The feature maps from all branches are subsequently fused and processed by convolutional layers for higher-level feature extraction and regression, generating an initial bathymetry prediction. Finally, boundary optimization is applied to produce the absolute bathymetry estimate.

2.3 Spatial Feature Branch

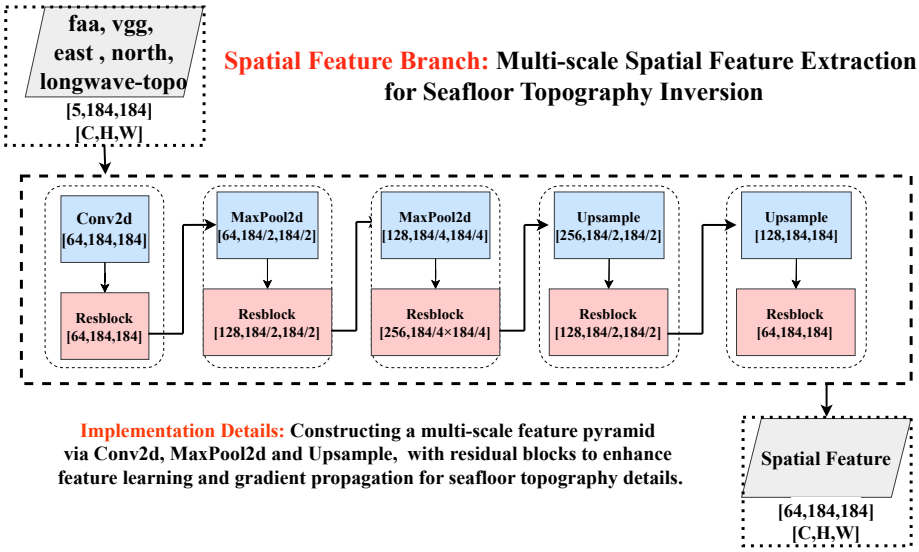


Fig. 3: The Spatial Feature Branch of SGL-CNN

The spatial feature branch employs an encoder-decoder architecture with residual connections to preserve low-frequency information as shown in Fig. 3. Given the input

tensor $\mathbf{X} \in \mathbb{R}^{5\times184\times184}$, an initial convolutional layer extracts fundamental features:

$$\mathbf{F_0} = \sigma(\texttt{Conv2d}(\mathbf{X})), \tag{1}$$

where σ is ReLU and the convolution uses 3×3 kernel . Within the encoder, two max-pooling operations are incorporated for downsampling to expand the receptive field:

$$\mathbf{F_{pool}} = \text{MaxPool}(\mathbf{F}, kernel = 2, stride = 2) \tag{2}$$

Correspondingly, the decoder employs two upsampling stages to restore spatial resolution.

$$\mathbf{F_{up}} = \text{BilinearUpsample}(\mathbf{F}, scale_factor = 2) \tag{3}$$

Moreover, to avoid the problem of gradient disappearance, residual connections that maintain feature integrity are strategically inserted: each followed by residual blocks to (a) Convolutional layers, (b) Downsampling operations, (c) Upsampling modules. The residual blocks are structured as follows,

$$\begin{aligned} \mathbf{F_k} &= \mathbf{Residual}(\mathbf{F_{k-1}}) \\ &= \sigma(\texttt{Conv2d}(\sigma(\texttt{Conv2d}(\mathbf{F_{k-1}})) + \mathbf{g}(\mathbf{F_{k-1}}). \end{aligned} \tag{4}$$

Here, $\mathbf{g}(\cdot)$ is join functions:

$$\mathbf{g}(\mathbf{F}) = \begin{cases} \mathbf{F}, & C_{in} = C_{out}, \\ \texttt{Conv2d}(\mathbf{F}), & \text{Otherwise}, \end{cases}$$

where the Conv2d kernel weight is $\mathbf{W_s} \in \mathbb{R}^{C_{out}\times C_{in}\times1\times1}$.

Finally, the spatial feature branch outputs a multiscale spatial feature representation $\mathbf{F}_{\text{spatial}} \in \mathbb{R}^{64\times H\times W}$, which captures local-scale topographic information for subsequent fusion with the frequency-based branches.

2.4 Global Frequency Feature Branch

The global frequency-domain branch analyzes the spectral distribution characteristics of gravity and long-wave topography as shown in Fig. 4. The processing pipeline comprises four stages, in which trapezoidal transitions reduce spectral leakage:

1. **Symmetric padding** is applied to mitigate boundary artifacts.

$$\mathbf{X}_{padded} = \mathbf{Pad}(\mathbf{X}_{in}, mode = replicate, padding = (8, 8, 8, 8)) \tag{5}$$

2. **2D Fast Fourier Transform (FFT)** is applied to obtain the spectra, which are decomposed into four frequency bands.

$$\mathcal{F}(\mathbf{X}) = \text{FFT2D}(\mathbf{X_{padded}}) \tag{6}$$

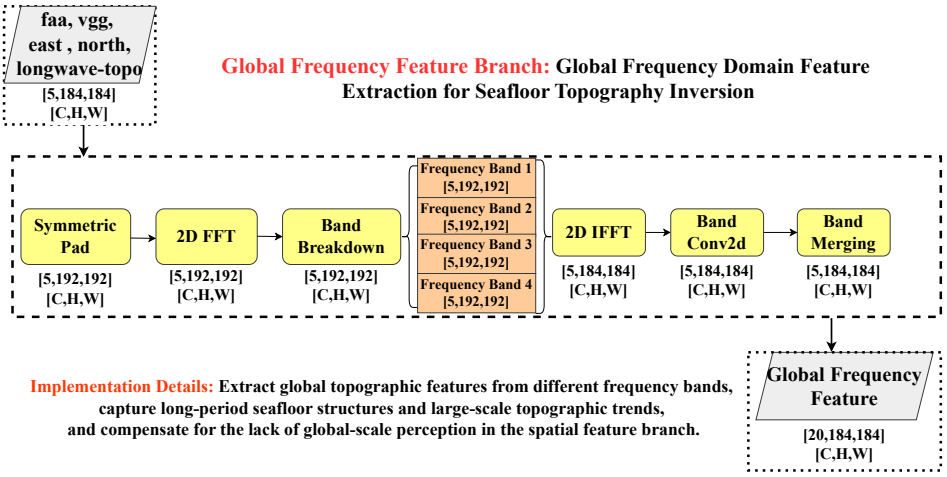


Fig. 4: The Global Frequency Feature Branch of SGL-CNN

$$M_i(f) = \begin{cases} \frac{f-(f_l-\Delta)}{\Delta} & f_l - \Delta \le f < f_l \\ 1 & f_l \le f < f_h \\ \frac{(f_h+\Delta)-f}{\Delta} & f_h \le f < f_h + \Delta \\ 0 & otherwise \end{cases} \tag{7}$$

where $f = \sqrt{f_x^2 + f_y^2}$ is the radial frequency, $f_l = i \cdot f_{max}/4$,$f_h = (i+1) \cdot f_{max}/4$ for $i = 0, 1, 2, 3$, and $\Delta = 0.1 f_{max}$. Here, $M_0(\cdot), M_1(\cdot), M_2(\cdot), M_3(\cdot)$ are used as band-pass filters.

3. **Band-specific processing**: Each frequency band undergoes the following:

   - Inverse FFT for the reconstruction of band-pass input features, as follows:

   $$\mathbf{X}_{i,c} = \mathcal{F}^{-1}(M_i \cdot \mathcal{F}(\mathbf{X}_c)), \tag{8}$$

   for $i \in \{1, 2, 3, 4\}$, which indicates the band-pass filters, and $c \in \{1, 2, 3, 4, 5\}$, which indicates the original input features, *faa*, *vgg*, *east*, *north* and *long_topo*.
   - Dual convolutional operations:

   $$\mathbf{F}_{i,c} = \texttt{Conv2d}(\sigma(\texttt{Conv2d}(\mathbf{X}_{i,c}))), \tag{9}$$

   where the Conv2d kernel weights are $\mathbf{W}_{i1}$ and $\mathbf{W}_{i2} \in \mathbb{R}^{1\times1\times3\times3}$, extracting features adaptively.

4. **Weighted fusion** integrates outputs from all frequency bands.

$$\mathbf{F}_{global} = \bigoplus_i (\texttt{Conv2d}(\bigoplus_c \mathbf{F}_{i,c})) \tag{10}$$

where $\oplus$ indicates channel splicing, and the Conv2d kernel weight is $\mathbf{W}_i \in \mathbb{R}^{1\times5\times1\times1}$ indicates the kernel weight for the convolutional operation of Conv2d. The output global frequency features are $\mathbf{F}_{global} \in \mathbb{R}^{20\times H\times W}$.

2.5 Local Frequency Feature Branch

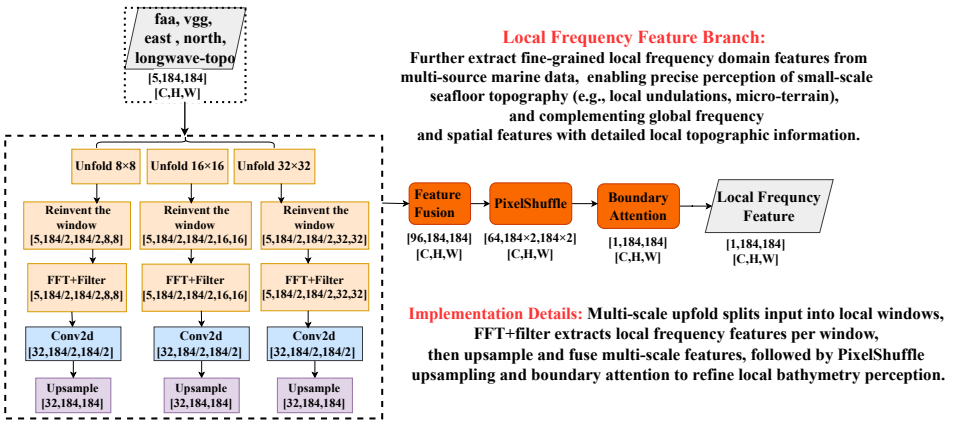


Fig. 5: The Local Frequency Feature Branch of SGL-CNN

Abrupt bathymetric changes generate high-frequency components in gravity anomalies, necessitating fine-grained local analysis. The local frequency branch therefore extracts multi-scale spectral features to establish correlations between local spectral energy distributions and seafloor topography, as shown in Fig. 5.

The processing pipeline consists of four stages:

1. **Multi-scale spectral extraction:** For each predefined window size $s \in \{8, 16, 32\}$, we extract overlapping local patches using a sliding window. The patch extraction is performed via an `Unfold` operation:

$$\mathbf{P}_s = \texttt{Unfold}(\mathbf{X}, \text{kernel_size} = s, \text{stride} = s/4, \text{padding} = s/2), \tag{11}$$

   where $\mathbf{X} \in \mathbb{R}^{5\times H\times W}$ is the input feature stack (faa, vgg, east, north, long_topo). For each scale s, this yields a collection of patches with spatial dimensions $s \times s$ and a total number of patches $L_s = \lceil (H + s/2)/(s/4) \rceil \times \lceil (W + s/2)/(s/4) \rceil$.
2. **Physics-aware feature learning:** For each patch, we compute its local amplitude spectrum via the 2D Fast Fourier Transform:

$$|\mathbf{A}_s| = |\mathcal{F}_{\text{local}}(\mathbf{P}_s)|\,. \tag{12}$$

   To extract physically interpretable frequency signatures, we apply a set of $M = 8$ learnable filters $\mathbf{W}_m^{(s)} \in \mathbb{R}^{1\times1\times s\times s}$ $(m = 1, \ldots, 8)$ to the amplitude spectrum. The

filtered energy for each filter group is obtained by summing over the frequency dimensions and averaging across the input channels:

$$\mathbf{E}_m^{(s)} = \frac{1}{5} \sum_{c=1}^{5} \sum_{u=0}^{s-1} \sum_{v=0}^{s-1} \left(|\mathbf{A}_s|_c \odot \mathbf{W}_m^{(s)} \right)_{u,v}, \tag{13}$$

where $\odot$ denotes element-wise multiplication. The resulting $\mathbf{E}_m^{(s)}$ has shape $[B, M, L_s]$ (or reshaped to a spatial grid $[B, M, H_s, W_s]$ with $H_s \times W_s = L_s$).

3. **Multi-scale feature reconstruction:** For each scale, we apply two convolutional layers to transform the energy features into a richer representation:

$$\mathbf{C}_s = \texttt{Conv2d}\big(\sigma(\texttt{Conv2d}(\mathbf{E}^{(s)})),\big), \tag{14}$$

where σ is ReLU and both convolutions use 3×3 kernels. The output $\mathbf{C}_s \in \mathbb{R}^{32 \times H_s \times W_s}$ is then bilinearly upsampled to the original input size $H \times W$. The upsampled features from all three scales are concatenated along the channel dimension, producing $\mathbf{U}_{\text{concat}} \in \mathbb{R}^{96 \times H \times W}$.

4. **Boundary refinement and residual enhancement:** The concatenated features are passed through a sub-pixel upsampling block that doubles the spatial resolution:

$$\mathbf{U} = \texttt{PixelShuffle}_2\big(\sigma(\texttt{Conv2d}(\mathbf{U}_{\text{concat}}, 256))\big), \tag{15}$$

where $\texttt{PixelShuffle}_2$ reduces the channel count by a factor of 4, yielding $\mathbf{U} \in \mathbb{R}^{64 \times 2H \times 2W}$. To match the original input dimensions, we bilinearly interpolate $\mathbf{U}$ back to $H \times W$ (denoted as $\tilde{\mathbf{U}} \in \mathbb{R}^{64 \times H \times W}$). A boundary attention module generates an edge-enhancement mask:

$$\mathbf{B} = \sigma\big(\texttt{Conv2d}(\sigma(\texttt{Conv2d}(\tilde{\mathbf{U}}, 32)), 1)\big), \tag{16}$$

where $\mathbf{B} \in \mathbb{R}^{1 \times H \times W}$. The final output combines the refined features with a residual connection:

$$\mathbf{F}_{\text{local}} = \tilde{\mathbf{U}} \odot (1 + \mathbf{B}) + \texttt{Conv2d}(\tilde{\mathbf{U}}, 64), \tag{17}$$

resulting in $\mathbf{F}_{\text{local}} \in \mathbb{R}^{64 \times H \times W}$.

3 Study Areas and Baseline Methods

To demonstrate the topography feature extraction capability of SGL-CNN, three representative areas in the Pacific Ocean were selected: Area 1 is a gently sloping abyssal plain with minimal bathymetric variation; Area 2 is a seamount complex exhibiting rugged bathymetry; and Area 3 is a trench system featuring complex topographical discontinuities. Fig. 6 presents their geographical distribution within the Pacific basin, while Fig. 7 displays the corresponding ETOPO1-derived bathymetric data in both planar and cross-sectional views.

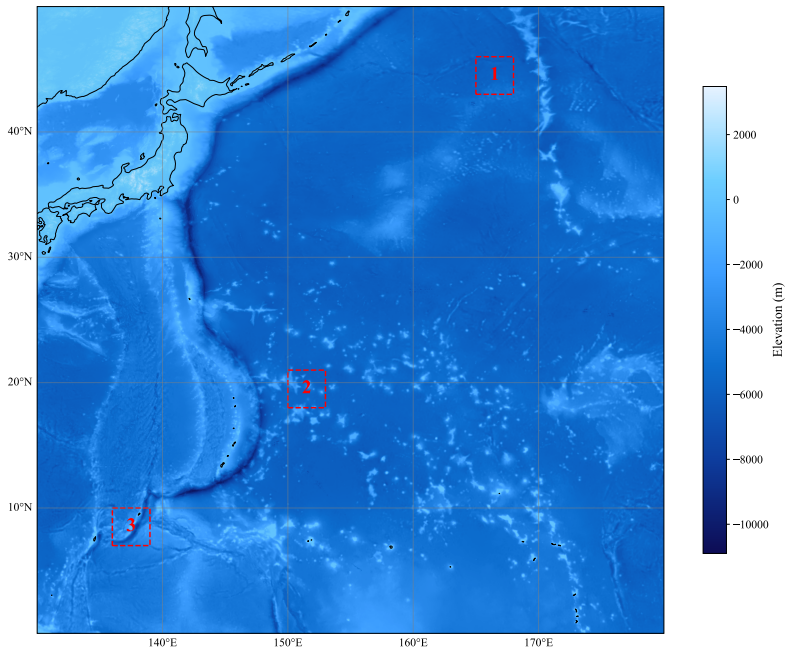
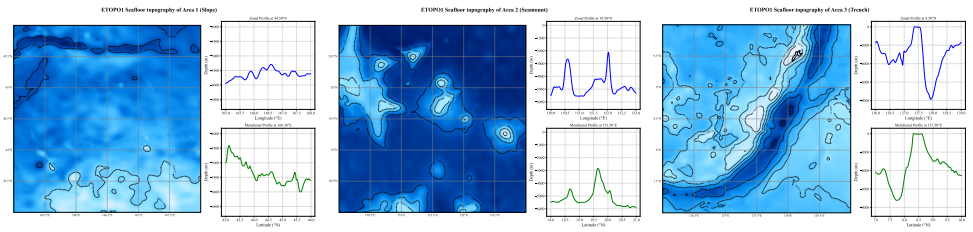


Fig. 6: Geographic Distribution of Study Areas in the Pacific Ocean (Area 1: High Latitude; Area 2: Mid Latitude; Area 3: Low Latitude.



(a) (b) (c)

Fig. 7: Morphological details of the study areas: Plan views and cross-sections along their central latitudinal and longitudinal axes (a) Area 1 (Slope); (b) Area 2 (Seamount); (c) Area 3 (Trench) .

And we further counted the basic information of the three regions, as shown in Tab. 1,we can conclude that Area 1 has a gentle terrain, while Area 2 and Area 3 have large undulations.

Table 1: Summary of Detailed Information for the Study Areas.

Study Areas	Latitude	Longitude	Min (m)	Max (m)	Mean (m)	Std (m)
Area 1	$43^\circ - 46^\circ$N	$165^\circ - 168^\circ$E	-6338	-4314	-5530	375
Area 2	$18^\circ - 21^\circ$N	$150^\circ - 153^\circ$E	-6089	-198	-5020	1035
Area 3	$7^\circ - 10^\circ$N	$136^\circ - 139^\circ$E	-8461	87	-3909	1475

3.1 Data Source and Preprocessing

Gravity anomalies.

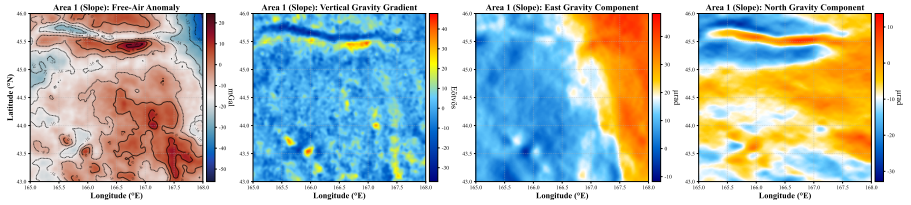
This study selected four gravity signal features as inputs: free-air gravity anomaly (*faa*), vertical gravity gradient (*vgg*), and the components of the deflection of the vertical (*east* and *north*). The data are sourced from version 32 of the gravity products released by the Scripps Institution of Oceanography, USA (https://topex.ucsd.edu/pub/global_grav_1min/). These four gravity signals reflect different spatial and frequency characteristics of seafloor topography.

In our analysis across three study regions (each $3^\circ \times 3^\circ$), each gravity signal is represented on a 184×184 grid. Figure 8 sequentially displays these four gravity signals for the three areas. It can be observed that *faa* reflects relatively mid-to-low frequency gravity characteristics, *vgg* retains high-frequency gravity characteristics, and the *east* and *north* components reveal directional characteristics of gravity. The SGL branches can capture multi-scale features from these input data, which are then used for bathymetry prediction.

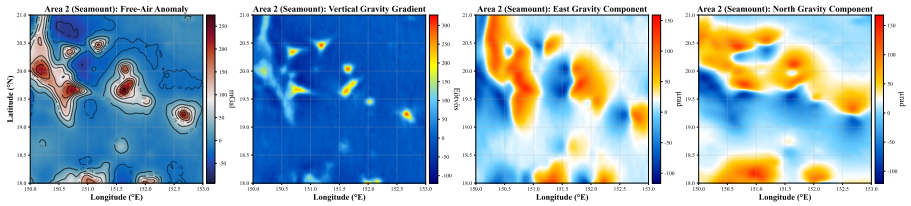
Shipborne bathymetric data.

Shipborne (single-beam and multi-beam) bathymetry utilized in this study were obtained from the National Oceanic and Atmospheric Administration (NOAA) bathymetric survey database (https://www.ngdc.noaa.gov/mgg/surveys/). Fig. 9 illustrates the spatial distribution of survey tracklines within the three study areas, which reveals uneven spatial distribution of single-beam and multi-beam survey tracklines, with coverage rates of 22.3% (Area 1), 34.4% (Area 2), and 50.1% (Area 3). Shipborne bathymetry were processed through the following workflow for neural network integration:

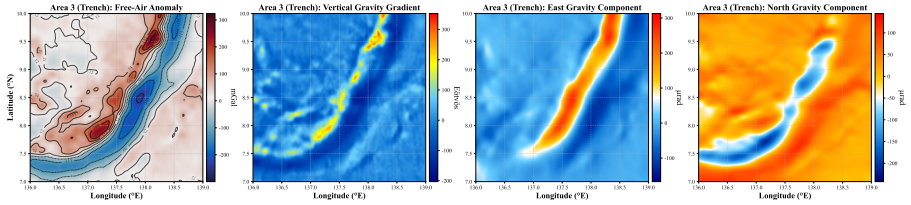
- **Step 1: Data Gridding.** Original trackline data exhibit heterogeneous resolution (low for single-beam vs. high for multi-beam). We defined a regular grid with the same resolution as the gravity anomalies (184×184 cells). For each grid cell, we collected all shipborne soundings that fall within that cell. Among those points, we assigned the depth of the sounding closest to the cell center as the grid value. If a



(a) Area 1: Slope



(b) Area 2: Seamount



(c) Area 3: Trench

Fig. 8: The gravity anomalies for the study areas from top to bottom are Area 1, Area 2, and Area 3, and from left to right are faa, vgg, east, and north within the area.

cell contained no ship measurements, it was assigned a value of zero.

$$B_{ij} = \begin{cases} \text{depth}\left(\underset{p \in \mathcal{P}_{ij}}{\text{argmin}} \, \| p - c_{ij} \| \right) & \text{if } \mathcal{P}_{ij} \neq \varnothing \\ 0 & \text{otherwise} \end{cases}$$

where c_{ij} is the center of grid cell (i, j), and $\mathcal{P}_{ij}$ is the set of ship soundings located within that cell.

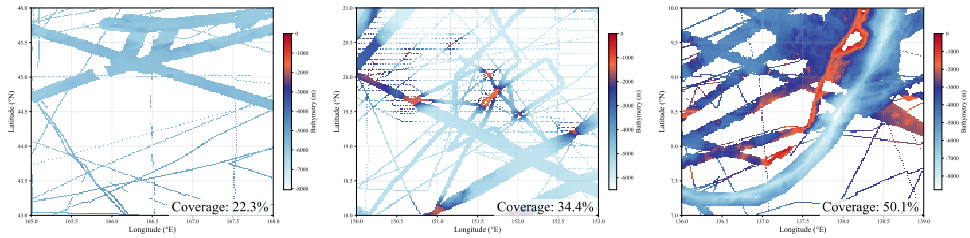
- **Step 2: Noise Removal.** Shipborne bathymetric data inevitably contain measurement noise and outliers. To remove gross errors, we performed a local statistical filter. For each grid cell, we considered ship soundings within a search radius equal to half the grid spacing (centered at the cell center). We computed the local mean μ_{ij} and standard deviation δ_{ij} of these points. Any sounding deviating by more than four times the local standard deviation from the local mean was identified as an outlier and removed. If no soundings existed within the search radius, we kept

the existing grid value unchanged (assuming no erroneous data in that area).

$$\mathcal{P}_{\text{clean}} = \left\{ p \in \mathcal{P}_{\text{local}}(c_{ij}) \;\middle|\; |\text{depth}_p - \mu_{ij}| \leq 4\delta_{ij} \right\}$$

where $\mathcal{P}_{\text{local}}(c_{ij})$ denotes ship soundings within the search radius around the cell center c_{ij}, and μ_{ij} and δ_{ij} are the mean and standard deviation of those points.

- **Step 3: Dataset Partitioning.** After gridding and noise removal, 20% of the non-zero grid points were used as the training set, and 80% were used as the test set.



(a) Area 1: Slope (b) Area 2: Seamount (c) Area 3: Trench

Fig. 9: The shipborne bathymetry for (a) Area 1; (b) Area 2; (c) Area 3.

3.2 Baseline Methods

ParkerO.

Based on potential field theory, the Parker–Oldenburg algorithm [11] iteratively recovers density interfaces from gravity anomalies in the frequency domain. We use `pyParkO`, a Python-based package developed by [25].

SAS.

[1] introduced a bandpass filter accounting for downward continuation and flexural isostasy. This approach establishes linear gravity-topography relationships within specific wavelength bands, combining band-limited bathymetry from gravity inversion and long-wavelength components from low-pass filtered shipborne bathymetry.

GGM.

The Gravity Geologic Method (GGM) was proposed by [15] as a method for bathymetry prediction in the spatial domain, utilizing the Bouguer formula to handle gravity anomalies in different frequency bands.

CNN.

Convolutional Neural Networks (CNNs) were proposed by [18] to treat 2-D gravity anomaly grids as spatially-referenced "pseudo-images" for input, with the gridded

bathymetry as the output. The convolutional layers are constructed to extract multi-scale information from the gravity anomalies, and the fully connected layers capture the nonlinear relationships between the gravity anomalies and bathymetry.

SGL-CNN.

We propose a method that integrates spatial, global frequency, and local frequency branches. The spatial branch extracts multi-scale features and long-wavelength trends, while the global frequency branch analyzes spectral distributions to establish frequency-dependent gravity–topography relationships. The local frequency branch captures high-frequency details via sliding-window spectral analysis with learnable filters. All three branches are fused to predict bathymetry.

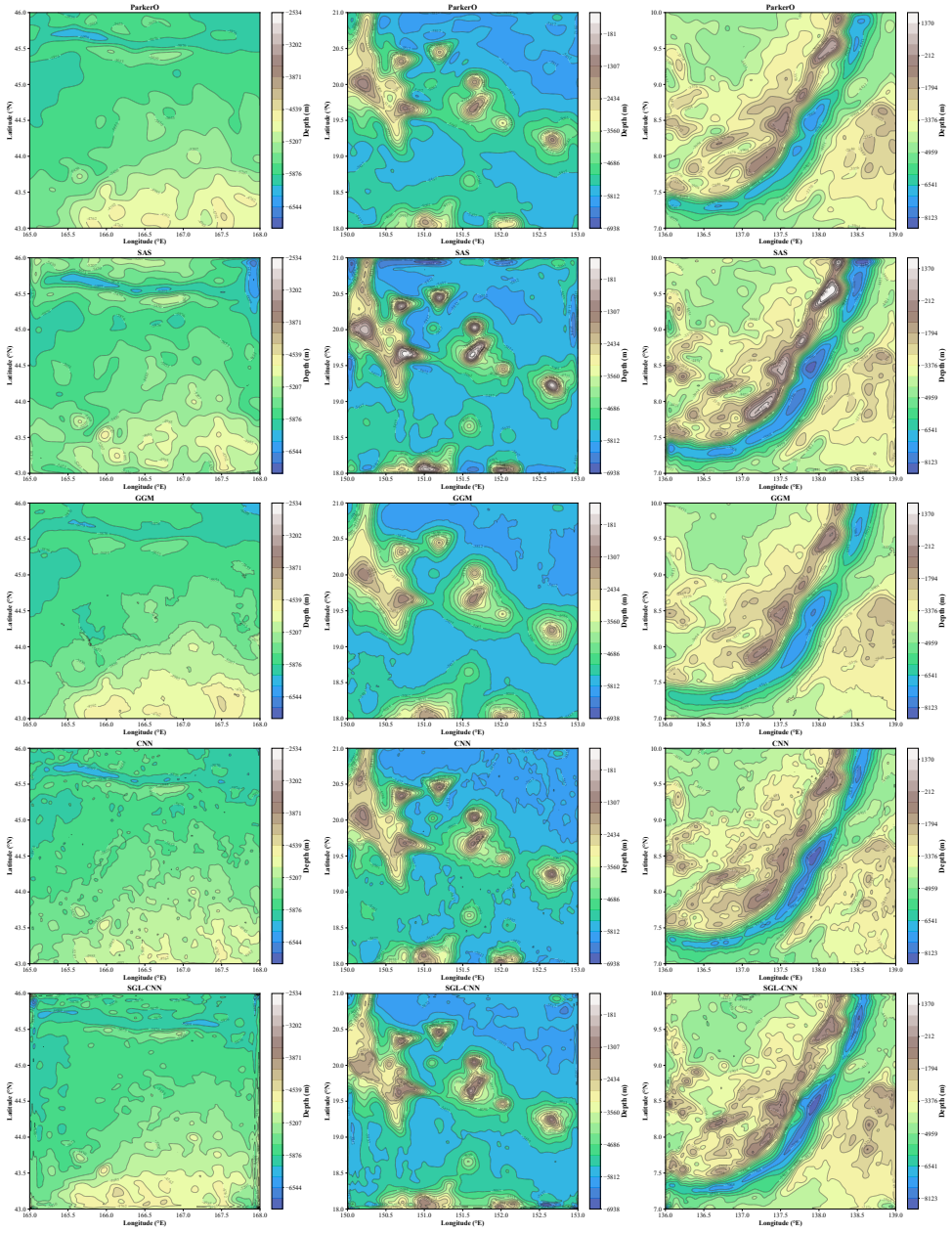
4 Results and Analysis

4.1 The Inversion Results Compared with Baseline Methods

Application of the SGL-CNN methodology across three morphologically distinct regions: slope (Area 1), seamount (Area 2), and trench (Area 3) generated high-resolution 2D bathymetric contour maps (Fig. 10) that demonstrate unprecedented topographic detail capture through five methods. All five methods generally succeeded in reconstructing the seafloor topography, with the SGL-CNN approach showing a slight advantage. In the slope area (Area 1), subtle microtopography (relief $\leq$ 20 m) is resolved, capturing both the gradual latitudinal depth gradient and minimal relief variations. In the seamount area (Area 2), the contour patterns delineate volcanic edifices, and buried abyssal hills are revealed, enabling comprehensive morphological characterization. In the trench area (Area 3), high-frequency plate boundary signals are precisely resolved, with contour lines tracing the Mariana Trench and identifying seamount clusters along the outer rise.

We further compare the error metrics (Tab. 2) of the residual differences between the bathymetric predictions of the five methods and the shipborne bathymetric points in three regions: Slope, Seamount, and Trench. ParkerO and SAS are frequency-domain methods, GGM and CNN are spatial-domain methods, while the proposed SGL-CNN is a dual-domain method that integrates both the spatial and frequency domains.

In Area 1 (Slope, characterized by flat topography), all five bathymetric prediction methods achieve high accuracy, with relatively low values across all error metrics. In Area 2 (Seamount, featuring complex topography), SGL-CNN demonstrates significantly lower values for the mean systematic bias (Bias), standard deviation (STD), mean absolute error (MAE), root mean square error (RMSE), and mean absolute percentage error (MAPE) compared to the other four methods. In the more complex Area 3 (Trench), the error metric values (Bias, STD, MAE, RMSE, MAPE) for SGL-CNN are nearly half those of the other methods. Compared to the single-domain methods, this demonstrates SGL-CNN's synergistic preservation of structural coherence and spectral sensitivity. As shown in Tab. 2, while traditional single-domain methods typically operate at a single scale within a specific domain, SGL-CNN effectively enhances the inversion of complex seafloor topography by leveraging multi-scale information from both the spatial and frequency domains.



(a) Area 1: Slope (b) Area 2: Seamount (c) Area 3: Trench

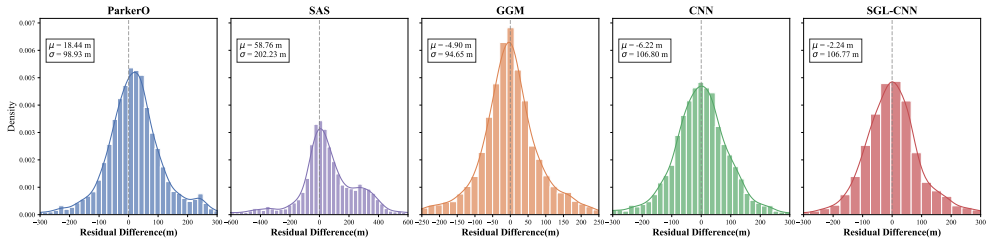
Fig. 10: Bathymetry predictions by five methods for (a) Area 1, (b) Area 2, and (c) Area 3 (Methods from top to bottom: ParkerO, SAS, GGM, CNN, SGL-CNN).

Table 2: Error metrics: comparison of five method predictions vs. shipborne bathymetry test data.

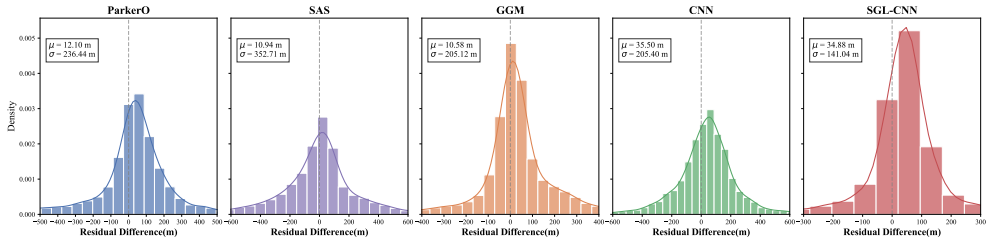
Survey Areas	Method	Bias(m)	STD(m)	MAE(m)	RMSE(m)	MAPE(%)
Area 1	**ParkerO**	18.4353	98.9365	73.5598	100.6312	1.2935
	SAS	58.7571	202.2512	150.6587	210.597	2.6545
	GGM	-4.8957	94.6546	65.7386	94.7731	1.1598
	CNN	-6.2223	106.8132	77.1303	106.9853	1.3829
	SGL-CNN	-2.2409	106.7779	75.1864	106.7925	1.3306
Area 2	**ParkerO**	12.0954	236.4573	156.1551	236.7533	4.2674
	SAS	10.9386	352.7289	222.8258	352.8789	6.3637
	GGM	10.5778	205.1312	125.2030	205.3924	3.4580
	CNN	35.5042	205.4117	150.3389	208.4463	3.7686
	SGL-CNN	34.8782	141.0521	95.2714	145.2927	2.3587
Area 3	**ParkerO**	69.0509	369.9491	289.0993	376.3243	7.7807
	SAS	-10.9472	460.1575	343.4781	460.2702	11.1124
	GGM	-11.8998	320.621	240.0661	320.8296	6.8526
	CNN	22.2768	317.5619	254.8355	318.3303	7.1817
	SGL-CNN	7.2674	196.8443	143.7948	196.9709	4.1013

Consequently, in regions with gentle topographic relief (like Area 1), both traditional single-domain/single-scale methods and the dual-domain/multi-scale SGL-CNN method yield high prediction accuracy. However, for bathymetric prediction in complex regions encompassing both low and high-frequency information (such as Areas 2 and 3), the comparative results between SGL-CNN and the other four methods highlight the importance of multi-scale feature extraction from the input gravity signals and long-wavelength topographic trend information within both the spatial and frequency domains. This integrated approach is crucial for constructing a more accurate nonlinear mapping to the seafloor topography, thereby enhancing both prediction accuracy and resolution

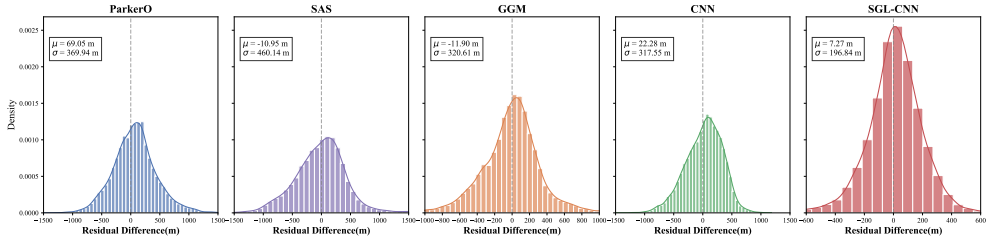
Additionally, we plotted the distribution histograms of residual differences for the five methods across the three regions and fitted the distribution density curves, as shown in Fig. 11. In the Slope region, due to relatively gentle topographic variations, the prediction accuracy of all five methods is high, and the residual differences approximately follow a normal distribution. In the Seamount region, compared to the other four methods, the SGL-CNN method shows a narrower range of residual differences, with a higher proportion of deviations within 100 meters, exhibiting a tendency towards a normal distribution. The ParkerO and SAS methods display certain tail characteristics in their residual differences, while the residual differences for the GGM and CNN methods have larger standard deviations, indicating lower prediction stability compared to SGL-CNN. In the Trench region, the distribution characteristics of residual differences are similar to those in the Seamount region: the SGL-CNN method has a narrower distribution range, approaching a normal distribution, whereas the other four methods have wider distribution ranges and exhibit heavy-tailed distributions.



(a) Area 1: Slope



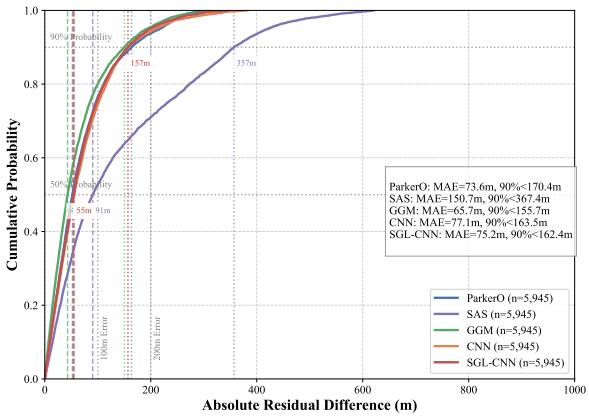
(b) Area 2: Seamount



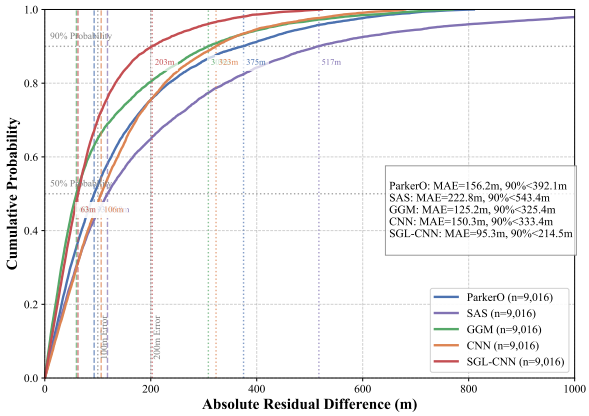
(c) Area 3: Trench

Fig. 11: The distribution of residual difference of five methods for (a) Area 1; (b) Area 2; (c) Area 3.

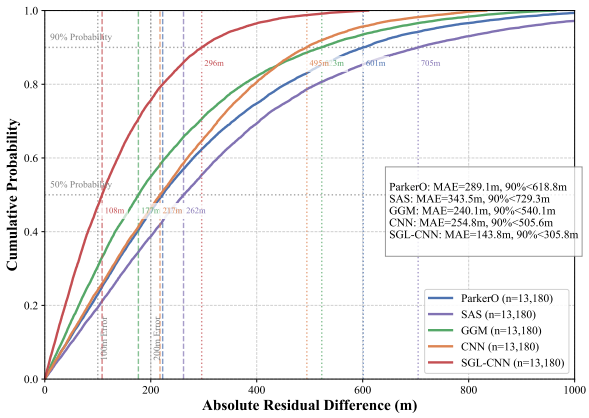
The cumulative absolute residual difference curve, shown in Fig. 12, further corroborates the aforementioned results: in the Slope region, all five methods exhibit high bathymetry prediction accuracy. In the more complex Seamount and Trench regions, the curve for SGL-CNN is positioned higher and rises more rapidly. In the Seamount region, 90% of the cumulative absolute residual differences are around 200 meters, while in the Trench region, 90% of the cumulative absolute residual differences are around 300 meters.



(a)



(b)



(c)

Fig. 12: The cumulative absolute residual difference curves of five methods for (a) Area 1; (b) Area 2; (c) Area 3.

4.2 The Performance of Bathymetry Prediction at Different Water Depth

In this section, we examine the influence of water depth on bathymetry prediction for the five methods. Using the true shipborne bathymetry from the test set as the horizontal axis and the residual difference between the ship values and the corresponding predicted values as the vertical axis, we display how the residual difference varies with water depth. Additionally, we further divide the true shipborne bathymetry of each region into five intervals and present the MAE, RMSE, and MAPE for each depth interval.

In the Slope region (Fig. 13), the residual difference range of the SAS method is larger compared to the other methods. The ParkerO, GGM, and CNN methods tend to overestimate in deep water and underestimate in shallow water. In contrast, the residual differences for the SGL-CNN method approximately follow a white noise distribution with a mean of zero as water depth varies.

In the Seamount and Trench regions (Fig. 14 and Fig. 15), the residual difference range of the SGL-CNN method is significantly lower than that of the other four methods and still follows a white noise distribution with water depth. The SAS and CNN methods exhibit wider residual difference ranges. The ParkerO and GGM methods continue to show overestimation in deep water and underestimation in shallow water, indicating a substantial influence of water depth.

All five methods incorporate long-wavelength topography in the bathymetry prediction process. The neural network-based methods, CNN and SGL-CNN, effectively learn the long-wavelength trends, resulting in residual differences that are unaffected by true water depth. In contrast, the residual differences for the traditional methods, ParkerO and GGM, are significantly influenced by true water depth, exhibiting overestimation in deep water and underestimation in shallow water. The SAS method, due to the low coverage of shipborne bathymetry in the selected regions during its construction, shows lower prediction accuracy compared to the other four methods, as evidenced by its wider residual differences.

We further divide the water depth range of each region into five intervals and observe the changes in MAE, RMSE, and MAPE across these depth intervals for the five methods.

In the Slope region as shown in Fig. 16, the MAE, RMSE, and MAPE for all five methods are higher in shallower water and lower in deeper water, with the lowest error metrics observed in the second depth interval. The error metrics for the SGL-CNN, GGM, and ParkerO methods exhibit small variations, while the SAS and CNN methods show larger fluctuations in their error metrics.

In the Seamount region as shown in Fig. 17, the prediction performance of all five methods is better in deeper water compared to shallower water. As the water depth decreases, the error metrics for the ParkerO, SAS, and GGM methods continuously increase, with a significant rise. The CNN and SGL-CNN methods also show some increase, but the rise is smaller, and the error metrics for SGL-CNN are significantly lower than those for CNN across all depth intervals.

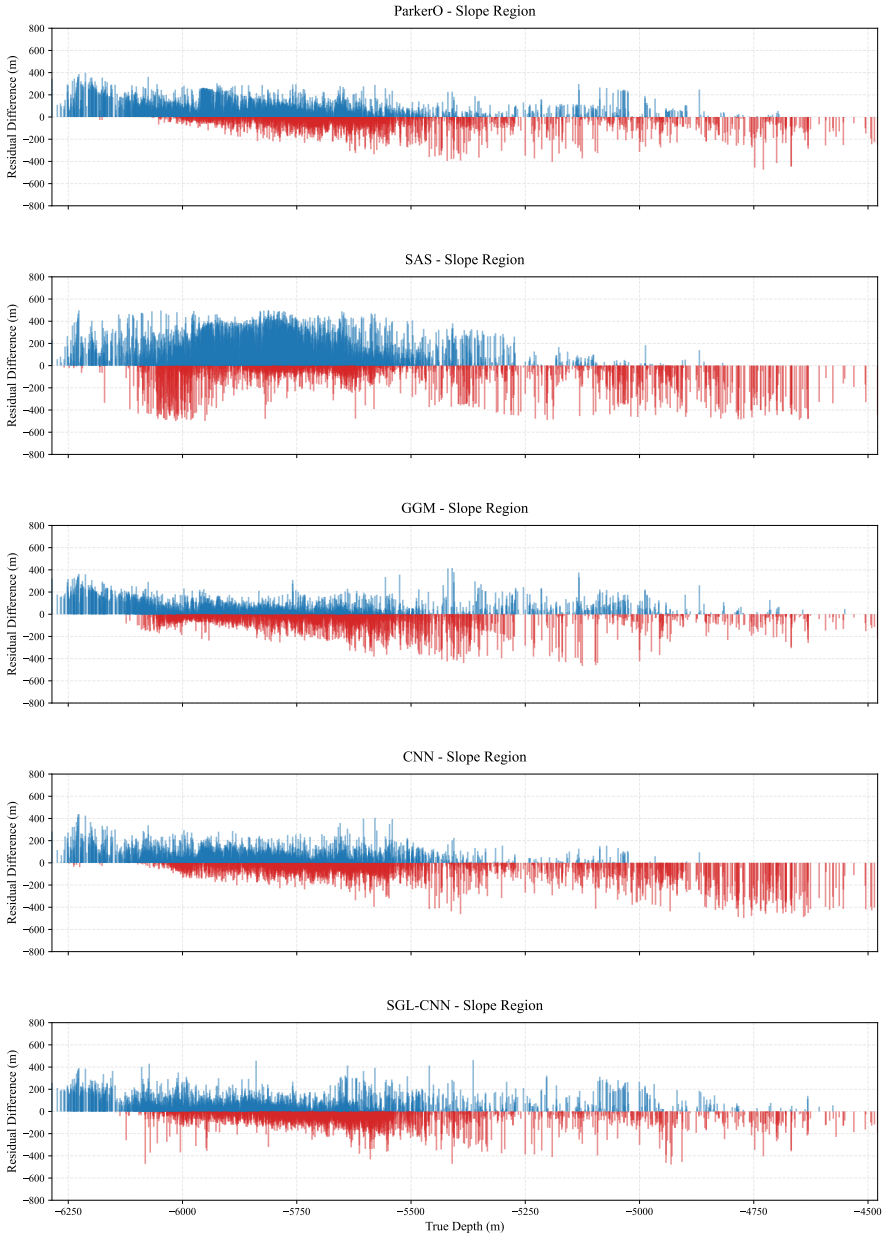


Fig. 13: The residual differences between the baseline methods' predictions and the shipborne bathymetry on the testing dataset along with water depths at Area 1.

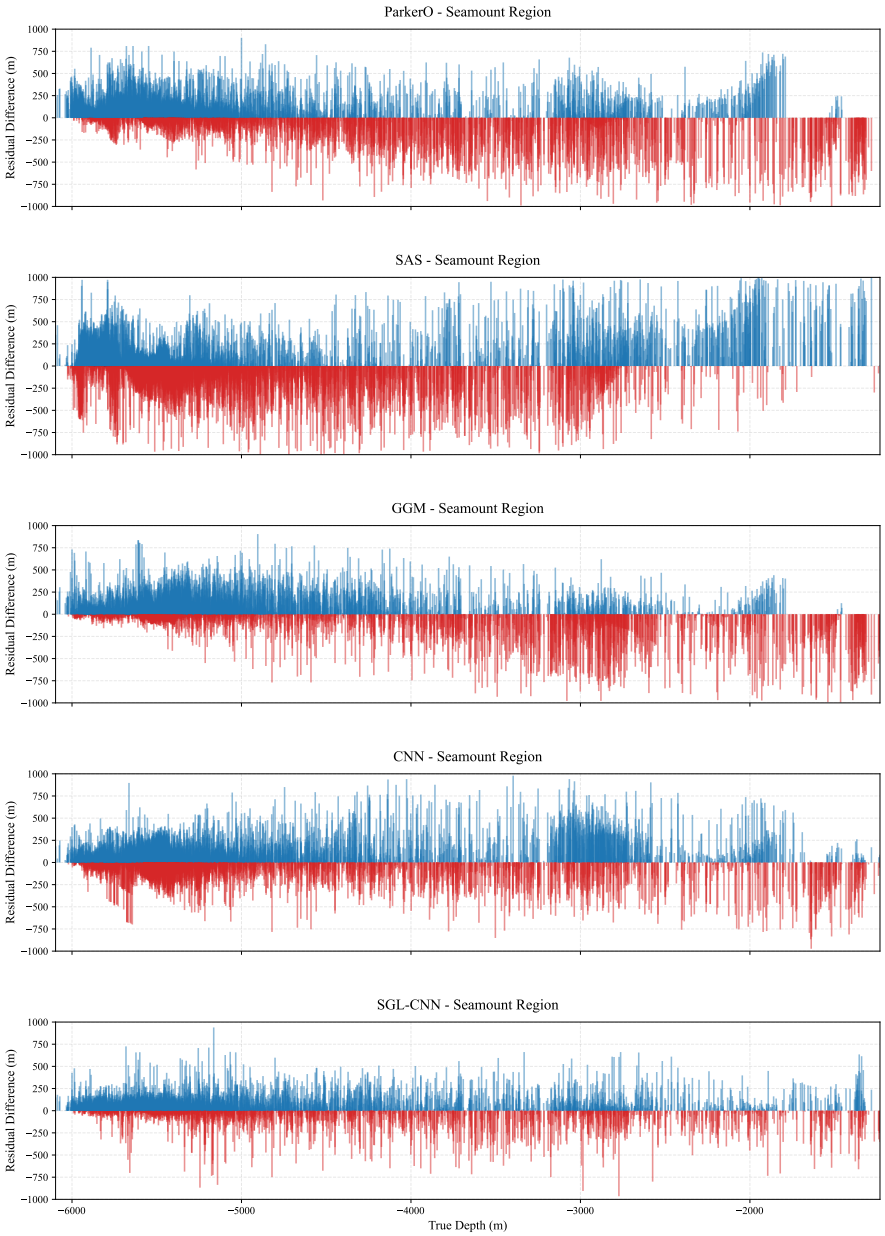


Fig. 14: The residual differences between the baseline methods' predictions and the shipborne bathymetry on the testing dataset along with water depths at Area 2.

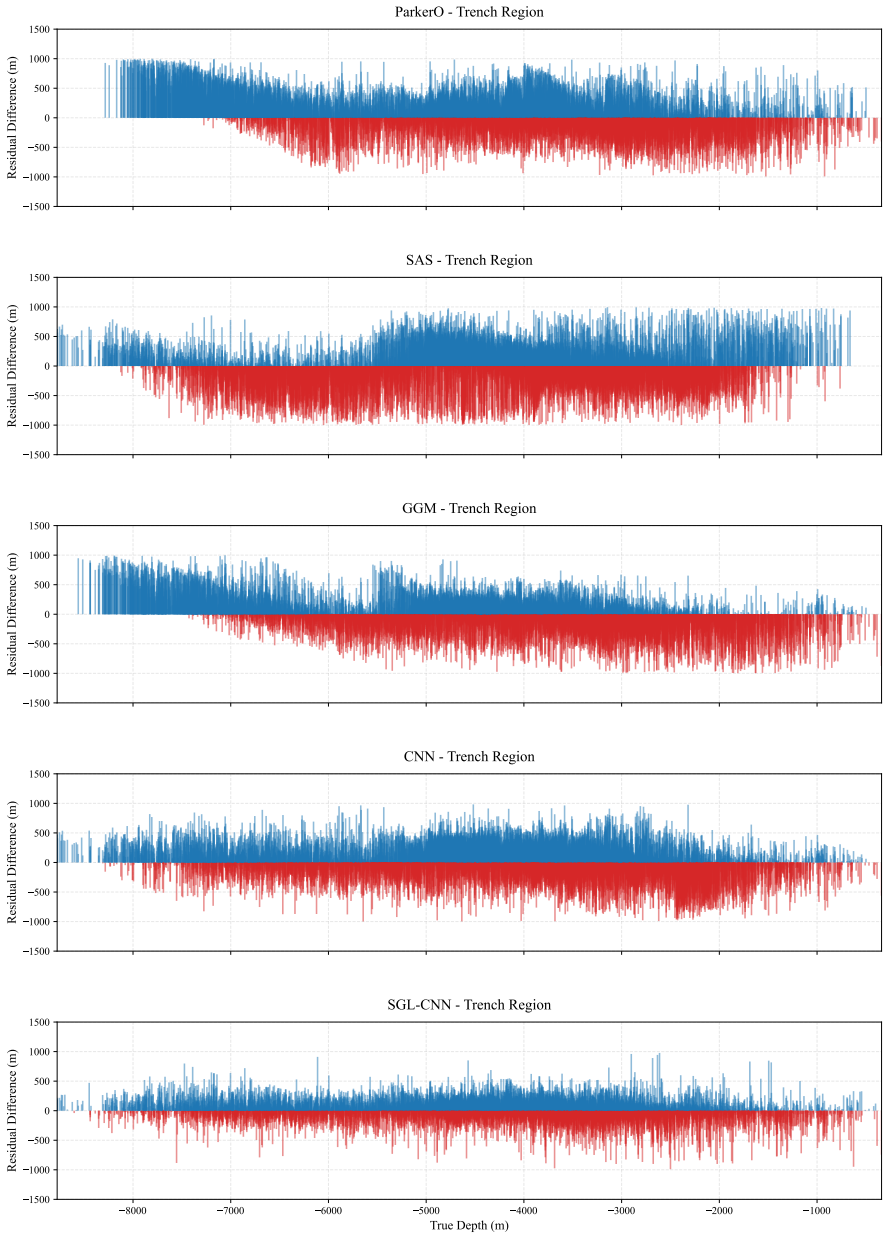


Fig. 15: The residual differences between the baseline methods' predictions and the shipborne bathymetry on the testing dataset along with water depths at Area 3.

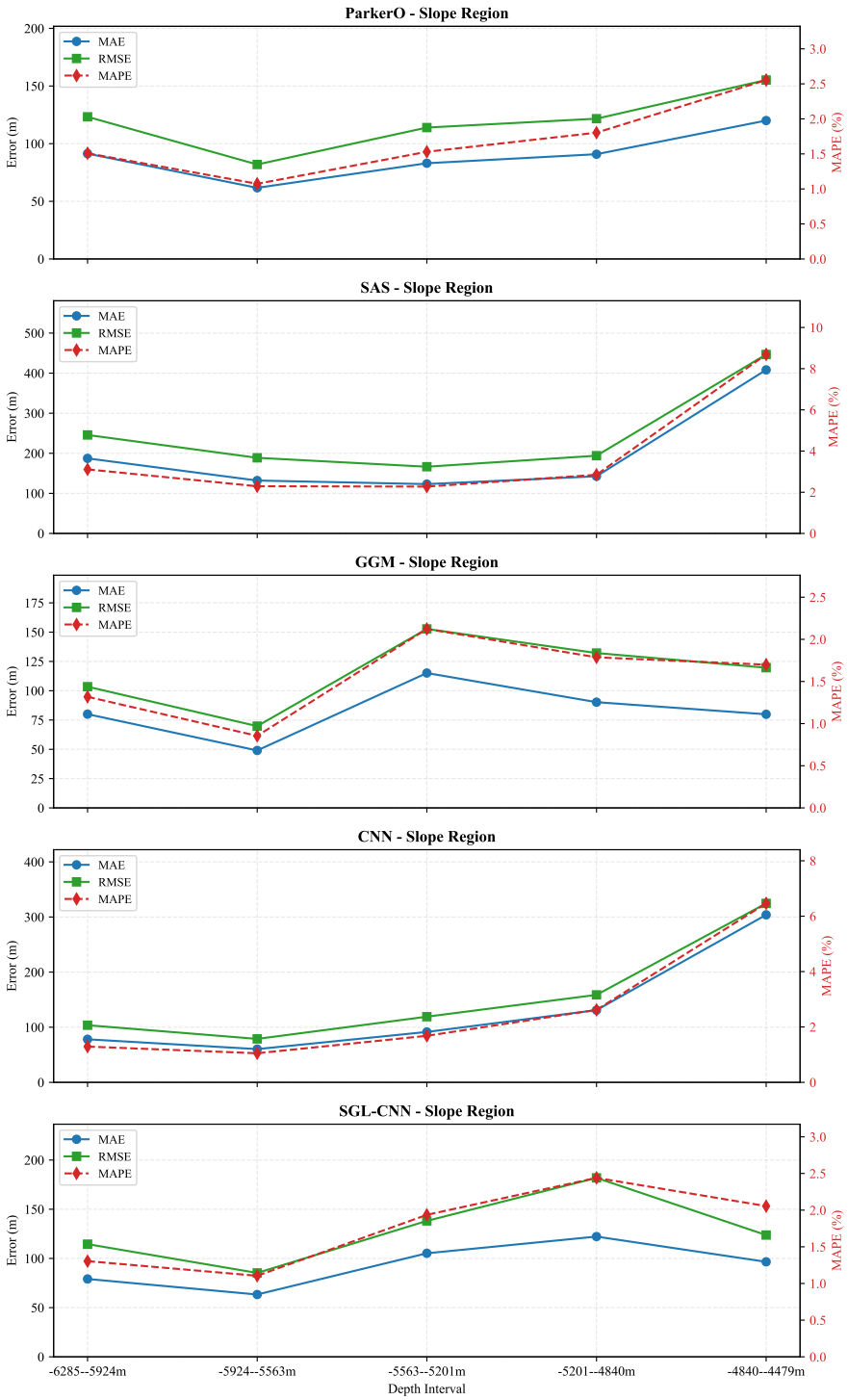


Fig. 16: Depth-dependent Performance at Area 1.

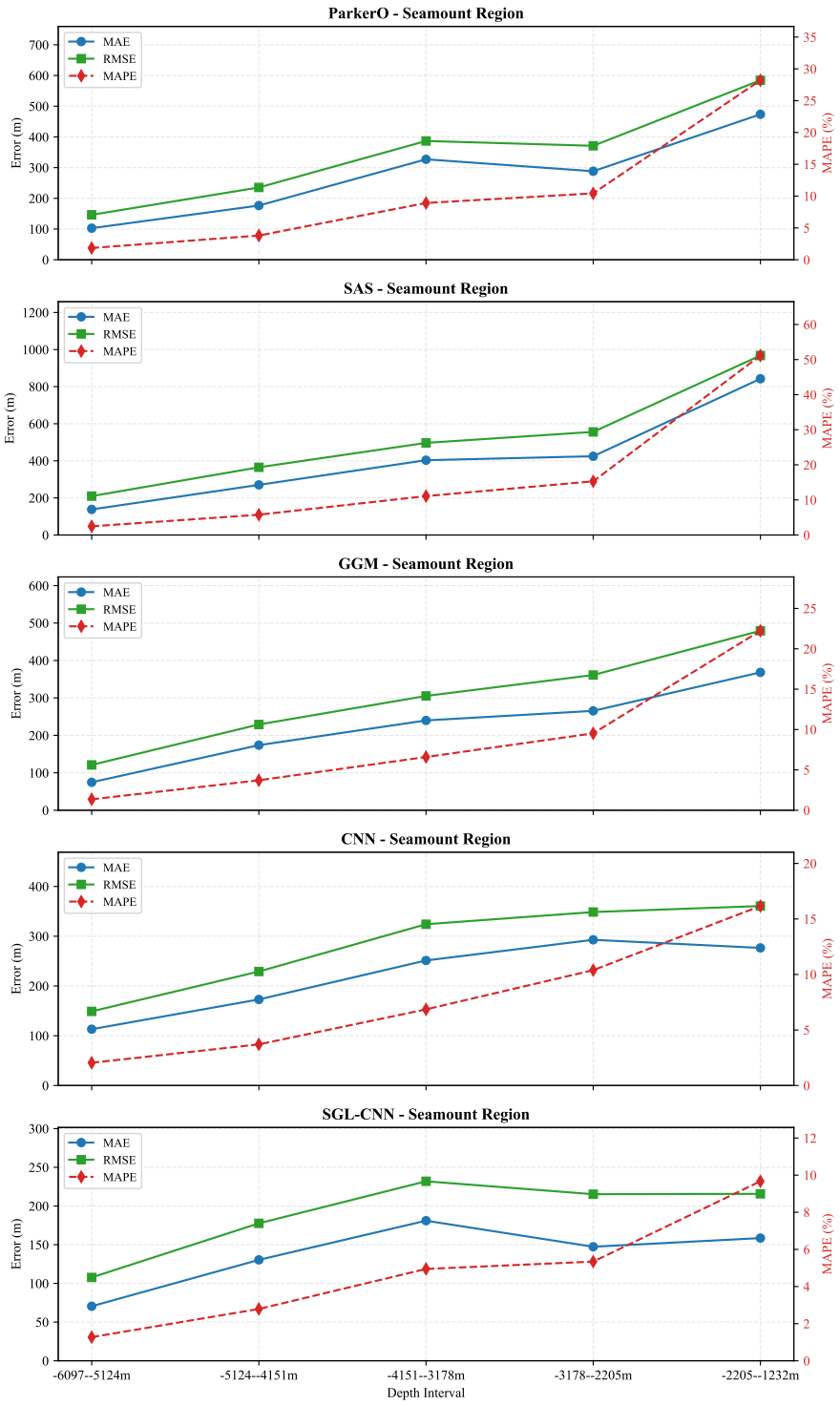


Fig. 17: Depth-dependent Performance at Area 2.

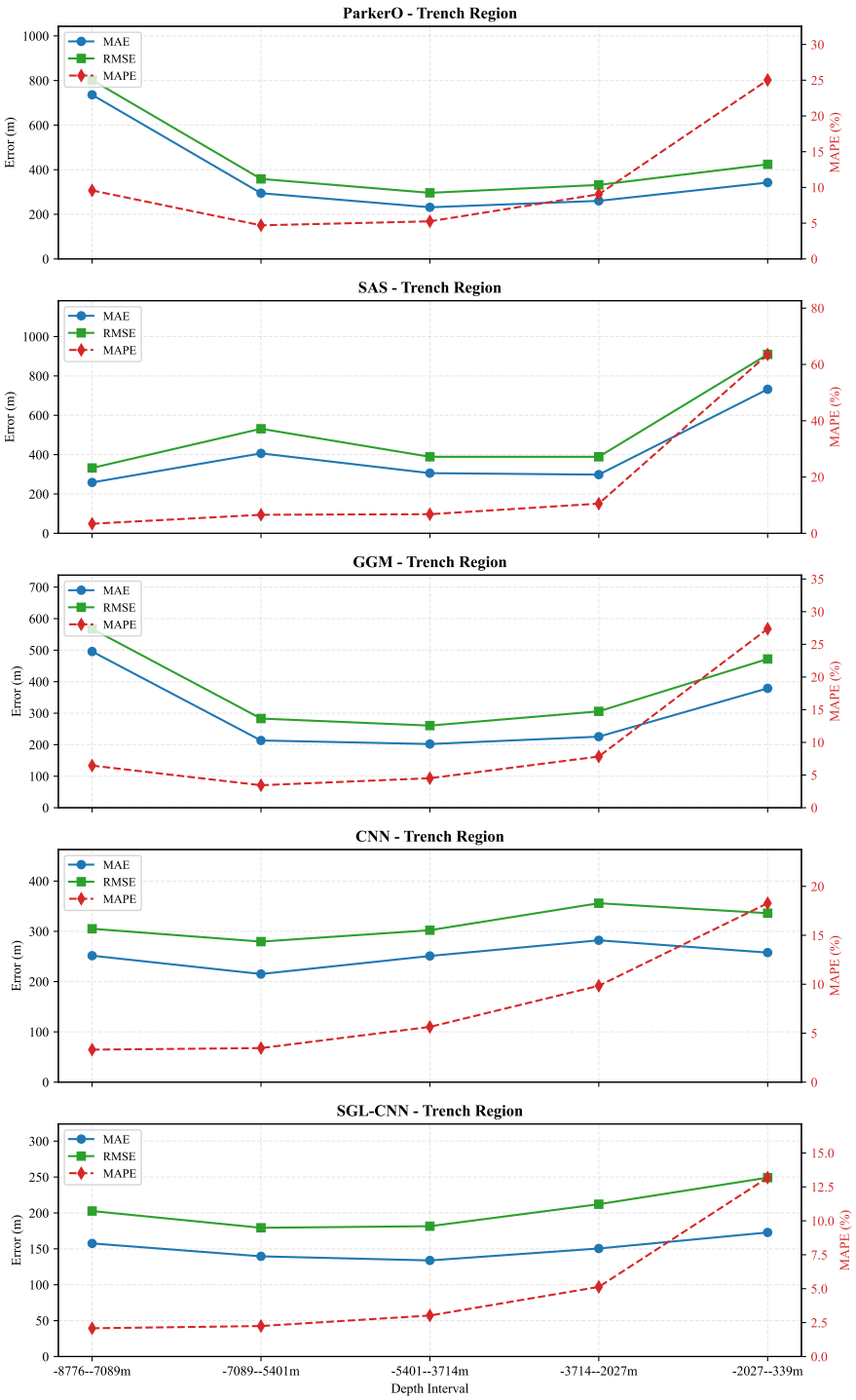


Fig. 18: Depth-dependent Performance at Area 3.

In the Trench region as shown in Fig. 18, where the maximum depth exceeds 8000 meters and the shallowest depth is around 2000 meters, the SGL-CNN method demonstrates stability in predictions across all depth ranges, with the smallest fluctuations in error metrics. The CNN method shows prediction performance second only to SGL-CNN. The ParkerO, SAS, and GGM methods exhibit high error metrics in both deep and shallow water, indicating considerable prediction biases.

In summary, the SGL-CNN method, which incorporates spatial and frequency domain gravity and trend information, is adaptable to bathymetric depth for seafloor topography inversion, particularly demonstrating stability in bathymetry prediction in complex terrain regions.

4.3 The analysis of Power spectral densities

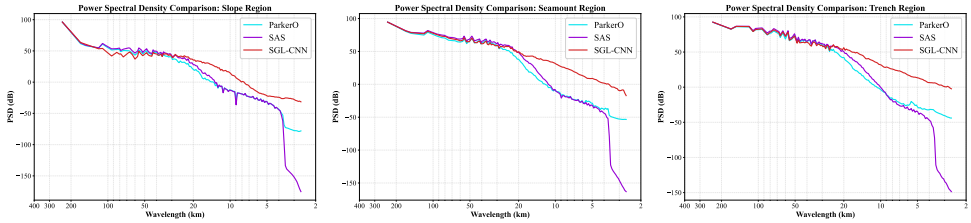
The power spectral density (PSD) analysis reveals the scale-dependent characteristics of different depth inversion methods. Figures 19 and 20 present the PSD analysis results for the seafloor topography regions. Fig. 19 compares the frequency domain methods, while Fig. 20 compares the spatial domain methods. Overall, the PSD values for all five methods are similar in the low-frequency region with wavelengths greater than 100 km, exhibiting similar attenuation characteristics, reflecting the self-similarity of the seafloor topography. In the 20-100 km range, the slope is generally lower, but the PSD values show considerable fluctuation. In the high-frequency region with wavelengths less than 20 km, the attenuation characteristics become steeper.

In the comparison of frequency domain methods as shown in Fig. 19 , SGL-CNN exhibits significantly higher PSD values in the high-frequency range below 20 km compared to ParkerO and SAS, particularly in the seamount and trench regions, indicating its ability to recover small-scale features. In the comparison of spatial domain methods as shown in Fig. 20, in the slope regions, SGL-CNN is roughly similar to GGM and CNN methods for wavelengths greater than 20 km. In the seamount and trench regions, the PSD values of SGL-CNN are slightly higher than those of GGM and CNN.

In summary, SGL-CNN demonstrates the optimal fidelity across the full spectrum, especially in the high-frequency range below 20 km. Traditional physical methods show significant limitations in recovering high-frequency details ($\lambda \leq 20km$). The SGL-CNN method, which extracts information from both domains for depth prediction, not only maintains the characteristic-preserving ability of spatial domain methods across various bands but also enhances the high-frequency detail recovery capability of frequency domain methods. This validates the advantage of the hybrid architecture in cross-scale seafloor topography modeling, providing a new paradigm for high-resolution depth inversion.

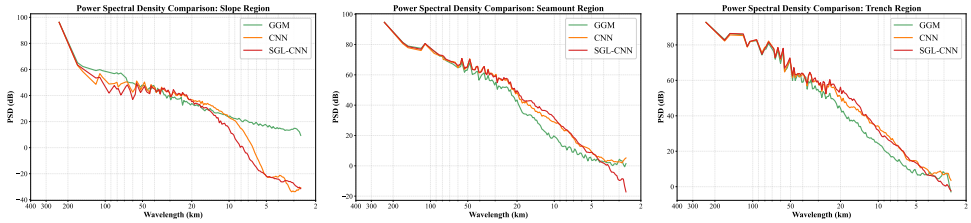
5 Conclusions

This study proposes a novel feature engineering framework, spatial global- and local-convolutional neural networks (SGL-CNN), for bathymetry prediction. The SGL-CNN network architecture primarily consists of three parts: a spatial domain branch that extracts multi-scale features of the input gravity signal and trend information; a global frequency domain branch that transforms the signal to the frequency domain via FFT,



(a) (b) (c)

Fig. 19: Power spectral densities of frequency methods for (a) Area 1; (b) Area 2 (c) Area 3.



(a) (b) (c)

Fig. 20: Power spectral densities of spatial methods for (a) Area 1; (b) Area 2 (c) Area 3.

performs band-pass filtering, and then converts it back to the spatial domain to extract global frequency domain features; and a local frequency domain branch that employs FFT within a multi-scale sliding window combined with a learnable filter to extract local frequency domain features.

We selected three regions with distinct topographic features (slope, seamount, and trench) to conduct bathymetry prediction experiments using SGL-CNN. The slope region features gentle topographic changes, with gravity signals dominated by long-wavelength components. The seamount region contains more medium- and short-wavelength components, while the trench region exhibits more complex multi-scale frequency band information. The bathymetry prediction results were compared with those obtained from ParkerO, SAS, GGM, and CNN methods. In the slope region, the prediction performance of all five methods is roughly the same; however, in the seamount and trench regions, the bathymetry prediction performance of SGL-CNN is superior to the other four methods.

By showcasing experimental results across different topographic regions and depths, we have demonstrated that the dual-domain architecture of SGL-CNN directly addresses the multi-scale wavelength distribution of complex seafloor topography: low-frequency (slope trends), medium-frequency (seamount bodies), and high-frequency (trench fracture zones). Its fusion mechanism, which integrates global constraints in the frequency domain and local optimization in the spatial domain, overcomes the

spectral truncation problem of single-domain methods in cross-scale topography inversion. This approach can provide valuable insights for constructing high-resolution seafloor topography.

Applicable Conditions and Limitations.

Due to the periodic boundary assumption inherent in the Fourier transform, the proposed method is best suited for regularly gridded data in mid- to low-latitude regions, where the grid cells have approximately uniform area. Its application to high-latitude areas requires caution, as the convergence of meridians and the resulting distortion in regular grids may introduce artifacts. Therefore, for constructing complex seafloor topography, the method is recommended for regions where the input gravity data are available on a uniformly spaced grid and where the effects of Earth's curvature are minimal. Future extensions could consider spherical harmonic transforms or adaptive grid techniques to overcome these limitations.

Funding

Our research is supported by the National Natural Science Foundation of China (No. 92358303) and the Humanities and Social Sciences Foundation of the Ministry of Education of China (Grant No. 25YJCZH242).

Acknowledgments

The authors thank Professor Songxi Chen for guiding this research. We express our sincere gratitude to the following institutions for their support of our research. The Scripps Institution of Oceanography is acknowledged for the gravity data and the NOAA National Centers for Environmental Information (NCEI) for the provision of shipborne bathymetric data.

Data and Code Availability

All data and the code developed for this work have been deposited in a Zenodo repository https://zenodo.org/records/19253304.

Conflict of Interest

The authors declare that they have no known competing financial interests or personal relationships that could have appeared to influence the work reported in this paper.

References

[1] Smith, W.H., Sandwell, D.T.: Bathymetric prediction from dense satellite altimetry and sparse shipboard bathymetry. Journal of Geophysical Research: Solid Earth **99**(B11), 21803–21824 (1994)

[2] Sandwell, D.T., Smith, W.H., Gille, S., Kappel, E., Jayne, S., Soofi, K., Coakley, B., Géli, L.: Bathymetry from space: Rationale and requirements for a new, high-resolution altimetric mission. Comptes Rendus. Géoscience **338**(14-15), 1049–1062 (2006)

[3] Zhao, F., Xu, Y., Zheng, N., Tu, Z., Yang, F.: Arpenn: an improved deep convolutional neural network for bathymetry inversion with integrated physical constraints. Geophysical Journal International **241**(2), 891–900 (2025)

[4] Sandwell, D.T., Goff, J.A., Gevorgian, J., Harper, H., Kim, S.-S., Yu, Y., Tozer, B., Wessel, P., Smith, W.H.: Improved bathymetric prediction using geological information: Synbath. Earth and Space Science **9**(2), 2021–002069 (2022)

[5] Harper, H., Sandwell, D.T.: Global predicted bathymetry using neural networks. Earth and Space Science **11**(3), 2023–003199 (2024)

[6] Annan, R.F., Wan, X.: Refined bathymetric prediction based on feature extraction of gravity field signals: Bathy-fe. Journal of Geophysical Research: Machine Learning and Computation **1**(3), 2024–000205 (2024)

[7] Weatherall, P., Marks, K.M., Jakobsson, M., Schmitt, T., Tani, S., Arndt, J.E., Rovere, M., Chayes, D., Ferrini, V., Wigley, R.: A new digital bathymetric model of the world's oceans. Earth and space Science **2**(8), 331–345 (2015)

[8] Olgiati, A., Balmino, G., Sarrailh, M., Green, C.: Gravity anomalies from satellite altimetry: comparison between computation via geoid heights and via deflections of the vertical. Bulletin géodésique **69**, 252–260 (1995)

[9] Sun, H., Feng, Y., Fu, Y., Sun, W., Peng, C., Zhou, X., Zhou, D.: Bathymetric prediction using multisource gravity data derived from a parallel linked bp neural network. Journal of Geophysical Research: Solid Earth **127**(11), 2022–024428 (2022)

[10] Parker, R.L.: The rapid calculation of potential anomalies. Geophysical Journal International **31**(4), 447–455 (1973)

[11] Oldenburg, D.W.: The inversion and interpretation of gravity anomalies. Geophysics **39**(4), 526–536 (1974)

[12] Mingda, O., Zhongmiao, S., Zhenhe, Z., Xiaogang, L.: Bathymetry prediction based on the admittance theory of gravity anomalies. Acta Geodaetica et Cartographica Sinica **44**(10), 1092 (2015)

[13] Wölfl, A.-C., Snaith, H., Amirebrahimi, S., Devey, C.W., Dorschel, B., Ferrini, V., Huvenne, V.A., Jakobsson, M., Jencks, J., Johnston, G., *et al.*: Seafloor mapping–the challenge of a truly global ocean bathymetry. Frontiers in Marine Science **6**, 283 (2019)

[14] Zhu, F., Li, J., Li, Y., Xu, J., Guo, J., Zhou, J., Sun, H.: Estimating seafloor topography of the south china sea using swot wide-swath altimetry data. IEEE Journal of Selected Topics in Applied Earth Observations and Remote Sensing (2025)

[15] Kim, J.W., Frese, R.R., Lee, B.Y., Roman, D.R., Doh, S.-J.: Altimetry-derived gravity predictions of bathymetry by the gravity-geologic method. Pure and Applied Geophysics **168**, 815–826 (2011)

[16] Hu, M., Li, J., Jin, T.: Bathymetry inversion with gravity-geologic method in emperor seamount. Geomatics and Information Science of Wuhan University **37**(5), 610–612 (2012)

[17] Liu, S., Wang, L., Liu, H., Su, H., Li, X., Zheng, W.: Deriving bathymetry from optical images with a localized neural network algorithm. IEEE Transactions on Geoscience and Remote Sensing **56**(9), 5334–5342 (2018)

[18] Annan, R.F., Wan, X.: Recovering bathymetry of the gulf of guinea using altimetry-derived gravity field products combined via convolutional neural network. Surveys in Geophysics **43**(5), 1541–1561 (2022)

[19] Yang, L., Liu, M., Liu, N., Guo, J., Lin, L., Zhang, Y., Du, X., Xu, Y., Zhu, C., Wang, Y.: Recovering bathymetry from satellite altimetry-derived gravity by fully connected deep neural network. IEEE Geoscience and Remote Sensing Letters **20**, 1–5 (2023)

[20] Kim, K.B., Kim, J.S., Yun, H.S.: Bathymetry estimation using machine learning in the ulleung basin in the east sea. Sensors and Materials **35**(9 (3)), 3351–3362 (2023)

[21] Wang, Q., Wu, Z., Wu, Z., Wang, M., Zhao, D., Jin, T., Zhao, Q., Qin, X., Liu, Y., Jiang, Y., *et al.*: Enhanced seafloor topography inversion using an attention channel 1d convolutional network based on multiparameter gravity data: Case study of the mariana trench. Journal of Marine Science and Engineering **13**(3), 507 (2025)

[22] Chen, X., Zhong, M., Sun, M., An, D., Feng, W., Yang, M.: Recovering bathymetry using bp neural network combined with modified gravity–geologic method: A case study in the south china sea. Remote Sensing **16**(21), 4023 (2024)

[23] Jiang, X., Guo, J., Lin, M., Sun, H., Jiang, T.: Enhanced gravity-geologic method to predict bathymetry by considering non-linear effects of surrounding seafloor topography. Geophysical Journal International **239**(1), 754–767 (2024)

[24] Serpelloni, E., Faccenna, C., Spada, G., Dong, D., Williams, S.D.: Vertical gps ground motion rates in the euro-mediterranean region: New evidence of velocity gradients at different spatial scales along the nubia-eurasia plate boundary.

Journal of Geophysical Research: Solid Earth **118**(11), 6003–6024 (2013)

[25] Wang, C., Hua, L., Zeng, J., Liu, X.: pyparko: A python implementation of the parker-oldenburg method for seafloor topography inversion from gravity anomalies. Computers & Geosciences, 106137 (2026)